

## Article

# Evaluation of Shear-Punched Surface Layer Damage in Three Types of High-Strength TRIP-Aided Steel

Koh-ichi Sugimoto <sup>1,\*</sup>, Shoya Shioiri <sup>1</sup> and Junya Kobayashi <sup>2</sup>

<sup>1</sup> Graduate School of Science and Technology, Shinshu University, Nagano 380-8553, Japan; mellow.pretty8330@gmail.com

<sup>2</sup> Graduate School of Science and Engineering, Ibaraki University, Hitachi 316-8511, Japan; junya.kobayashi.jkoba@vc.ibaraki.ac.jp

\* Correspondence: btxpr049@ymail.ne.jp

**Abstract:** The damage properties in the shear-punched surface layer, such as the strain-hardening increment, strain-induced martensite fraction, and initiated micro-crack/void characteristics at the shear and break sections, were experimentally evaluated to relate to the stretch-flangeability in three types of low-carbon high-strength TRIP-aided steel with different matrix structures. In addition, the surface layer damage properties were related to the mean normal stress developed on shear-punching and microstructural properties. The shear-punched surface damage of these steels was experimentally confirmed to be produced under the mean normal stress of negative to 0 MPa. TRIP-aided bainitic ferrite (TBF) steel had the smallest surface layer damage, featuring a significantly suppressed micro-crack/void initiation. This was due to the fine bainitic ferrite lath matrix structure, a low strength ratio of the second phase to the matrix structure, and the high mechanical stability of the retained austenite. On the other hand, the surface layer damage of TRIP-aided annealed martensite (TAM) steel was suppressed next to TBF steel and was smaller than that of TRIP-aided polygonal ferrite (TPF) steel. The surface layer damage was also characterized by a large plastic strain, a large amount of strain-induced martensite transformation, and a relatively suppressed micro-crack/void formation, which resulted from an annealed martensite matrix and a large quantity of retained austenite. The excellent stretch-flangeability of TBF steel might be caused by the suppressed micro-crack/void formation and high crack propagation/void connection resistance. The next high stretch-flangeability of TAM steel was associated with a small-sized micro-crack/void initiation and high crack growth/void connection resistance.

**Keywords:** advanced high-strength steel; shear-punching; surface layer damage; mean normal stress; microstructure



**Citation:** Sugimoto, K.-i.; Shioiri, S.; Kobayashi, J. Evaluation of Shear-Punched Surface Layer Damage in Three Types of High-Strength TRIP-Aided Steel. *Metals* **2024**, *14*, 531. <https://doi.org/10.3390/met14050531>

Academic Editors: Haijiang Hu and Junyu Tian

Received: 20 March 2024

Revised: 28 April 2024

Accepted: 29 April 2024

Published: 30 April 2024



**Copyright:** © 2024 by the authors. Licensee MDPI, Basel, Switzerland. This article is an open access article distributed under the terms and conditions of the Creative Commons Attribution (CC BY) license (<https://creativecommons.org/licenses/by/4.0/>).

## 1. Introduction

The first-, second-, and third-generation advanced high-strength steels (AHSSs) have been applied to automobiles to reduce weight and improve crash safety performance [1–7]. These formable AHSSs are classified by strength grade, matrix structure, and plasticity mechanism (transformation-induced plasticity (TRIP)/twinning-induced plasticity (TWIP), which is mainly controlled by stacking fault energy of austenite phase), as follows.

- The first-generation AHSS: ferrite-martensite/bainite dual-phase (DP) [8–14], complex phase [12,13], TRIP-aided polygonal ferrite (TPF) [10,15–20], and TRIP-aided annealed martensite (TAM) [21,22] steels
- The second-generation AHSS: high manganese TWIP steel [23–25],
- The third-generation AHSS: TRIP-aided bainitic ferrite (TBF) [21,26–29], carbide-free bainitic (CFB) [30,31], quenching and partitioning (Q and P) [10,28,29,32–35], medium Mn (MMn) [36,37], and TRIP-aided martensitic (TM) [26] steels.

These AHSSs are characterized by excellent stretch-formability (maximum stretch height) [12,15–18,21–23,26–28,34,36] and stretch-flangeability (hole expansion ratio) [8,10–15,17,18,20–27,29–33,35–37], as shown in Figure 1 [21,22,26], as well as good deep drawability (limiting drawing ratio) [16,18,23] and bendability (minimum bending radius) [12,15,18,19,21]. These cold formabilities are evaluated under various stress states or mean normal stress states. According to Hiwatashi et al. [16] and Takahashi [18], an equibiaxial tension on stretch-forming enhances the strain-induced martensite transformation in TPF steel because of increased expansion strain. Many researchers have investigated the micro-crack/micro-void initiation [17,21] and growth [20,29] behaviors in regard to shear-punching and the stretch-flangeability in TPF and TAM steels. Furthermore, Sugimoto et al. also reported that the stretch-flangeability of TBF steel [27] is mainly controlled by the surface layer damage on shear-punching and crack growth and/or void connection on hole-expanding.

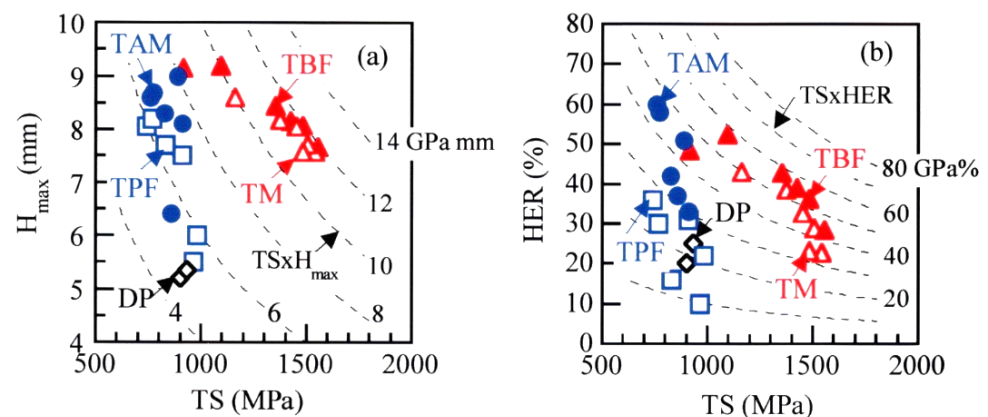


**Figure 1.** (a) Maximum stretch height–tensile strength ( $H_{\max}$ –TS) and (b) hole expansion ratio–tensile strength (HER–TS) relations in 0.15C–0.25Si–1.70Mn dual-phase (DP) steel, reprinted from [26], 0.2C–1.5Mn–Si–Al–Nb–Mo TRIP-aided polygonal ferrite (TPF) and TRIP-aided annealed martensite (TAM) steels, reprinted from [21,22], and 0.20C–1.5Si–1.5Mn–0.05Nb TRIP-aided bainitic ferrite (TBF) and TRIP-aided martensitic (TM) steels, reprinted from [26]. This figure is redrawn using the results of Refs. [21,22,26].

As the stress state near the sheared surface on shear-punching is complex [38], it is difficult to estimate the shear-punched surface layer damage. Sugimoto et al. [39] found that the mean normal stress significantly controls these behaviors in the TPF, TAM, and TBF steels with different matrix structures and retained austenite characteristics. Also, these behaviors are influenced by microstructural properties, such as the matrix structure, retained austenite characteristics, and second phase properties, such as martensite–austenite (MA) phase, strain-induced martensite, etc. However, no research has compared the shear-punched surface layer damage and related the damage to mean normal stress and microstructural properties in TPF, TAM, and TBF steels.

This research experimentally investigates the damage properties in the shear-punched surface layer, such as the strain-hardening increment, strain-induced martensite fraction, and initiated micro-crack/void characteristics, at the shear and break sections on shear-punching in low-carbon TPF, TAM, and TBF steels to relate to the stretch-flangeability. Additionally, the damage properties in the surface layer were related to the mean normal stress developed on shear-punching and the microstructural properties, such as the matrix structure, retained austenite characteristics, strength ratio of the second phase to the matrix, etc. In addition, the surface damage properties were related to the stretch-flangeability.

## 2. Experiments

Low-carbon steel, with a chemical composition seen in Table 1, was prepared as a 100 kg slab by vacuum melting. The slab was hot-rolled to a 13 mm diameter at a finish

temperature of 850 °C. Tensile specimens (JIS-14A, 25 mm gauge length, 5 mm diameter) parallel to the rolling direction were machined from the hot-rolled bars. Hole punching samples, all featuring a 10 mm width, 50 mm length, and 1.2 mm thickness, were sliced from a 1/2 radius of the hot-rolled bars in the longitudinal direction (Figure 2a). Three kinds of heat treatments, shown in Figure 3, were applied to the samples to produce the TPF, TAM, and TBF steels. In this research, an austenitizing temperature of 910 °C, intercritical annealing temperature of 780 °C (between  $A_3$  and  $A_1$ ), and isothermal transformation temperature of 375 °C (for TPF and TAM steels) or 410 °C ( $>M_s$ , for TBF steel) were adopted to obtain the maximum retained austenite fraction.

**Table 1.** Chemical composition (mass%) and measured martensite-start ( $M_s$ ) and -finish ( $M_f$ ) temperatures (°C) of slab used.

C	Si	Mn	P	S	Al	Nb	Cr	Mo	N	$M_s$	$M_f$
0.18	1.48	1.49	0.004	0.003	0.043	0.05	1.02	0.20	0.001	407	292

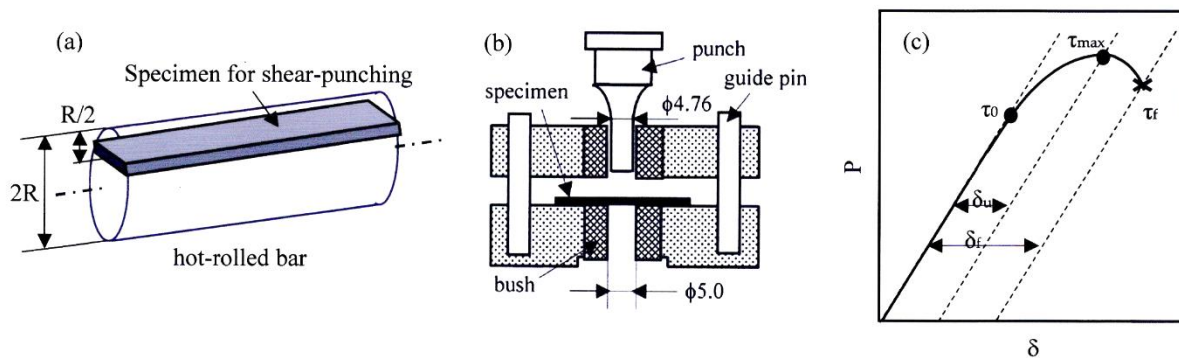


**Figure 2.** (a) Sampling location of the shear-punching thin specimens (10 mm width, 50 mm length, and 1.2 mm thickness), (b) dimensions of the shear-punching die set, and (c) definition of the shear-punching parameters on the shear-punching load–stroke ( $P$ – $\delta$ ) curve.  $R$ : a radius of the hot-rolled bar. Die set was made from JIS-SKD61 hot die steel.

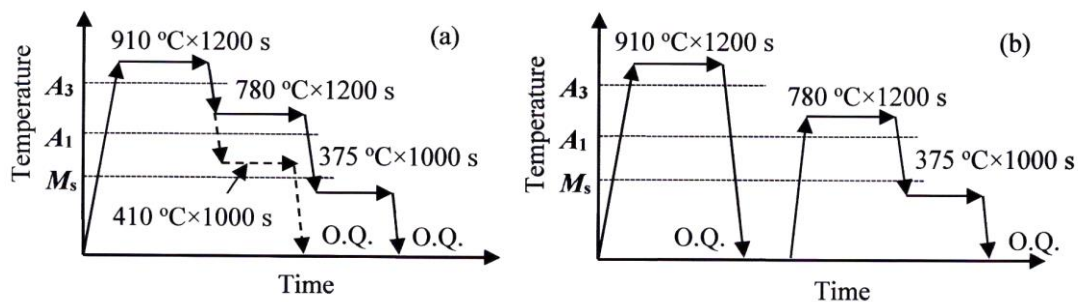


**Figure 3.** Heat treatment diagrams of (a) TPF (solid lines) and TBF (dotted lines) and (b) TAM steels. These heat treatments were carried out in salt and oil baths. O.Q.: Quenching in an oil bath at 50 °C.

The microstructure of the steels was observed at a 1/2 radius of the hot-rolled bars by a field-emission scanning electron microscopy (FE-SEM; JSM-6500F, JEOL Ltd., Akishima, Tokyo, Japan), which was performed using an instrument equipped with an electron backscatter diffraction system (EBSD; OIM system, TexSEM Laboratories, Inc., Provo, UT, USA). The EBSD analysis was conducted in an area of  $50 \times 50 \mu\text{m}^2$  with a beam diameter of 1.0  $\mu\text{m}$  and a beam step size of 0.05  $\mu\text{m}$  operated at an acceleration voltage of 25 kV. The specimens for FE-SEM–EBSD analysis were first ground with alumina powder and colloidal silica, and ion-thinning was then carried out.

The retained austenite characteristics, equivalent plastic strain, hardness, and micro-crack/void formation behavior on the surface and cross-section were evaluated in the

shear-punched surface layer. The retained austenite characteristics of the steels were evaluated by an X-ray diffractometer (RINT2000, Rigaku Co., Akishima, Tokyo, Japan). The cross-section of the shear-punched samples was electro-polished after being ground with emery paper (#1200) and alumina powder, followed by Nital etching. The volume fraction of the retained austenite phase ( $f_\gamma$ , vol%) was quantified from the integrated intensity of the (200) $\alpha$ , (211) $\alpha$ , (200) $\gamma$ , (220) $\gamma$ , and (311)  $\gamma$  peaks obtained by X-ray diffractometry using Mo-K $\alpha$  radiation [40]. The carbon concentration in the retained austenite ( $C_\gamma$ , mass%) was estimated from the empirical equation proposed by Dyson and Holmes [41]. To accomplish this, the lattice constant of retained austenite was determined from the (200) $\gamma$ , (220) $\gamma$ , and (311) $\gamma$  peaks of the Cu-K $\alpha$  radiation.

An equivalent plastic strain ( $\bar{\epsilon}_p$ ) in the punched surface layer was estimated from a half-width (HW) of X-ray (211) $\alpha$  peak of the Cu-K $\alpha$  radiation [42] through the relationship between the HW and  $\bar{\epsilon}_p$  known as the Williamson-Hall equation [43,44]. In the present TPF, TAM, and TBF steels plastically deformed in tension, torsion, and compression, the HW- $\bar{\epsilon}_p$  relation is shown in Figure 4 [39]. The hardness was measured using a Vickers microhardness tester (DUH-201H, Shimadzu Co., Kyoto, Japan) with a load of 0.98 N. Micro-crack/void formation behavior was observed by FE-SEM.

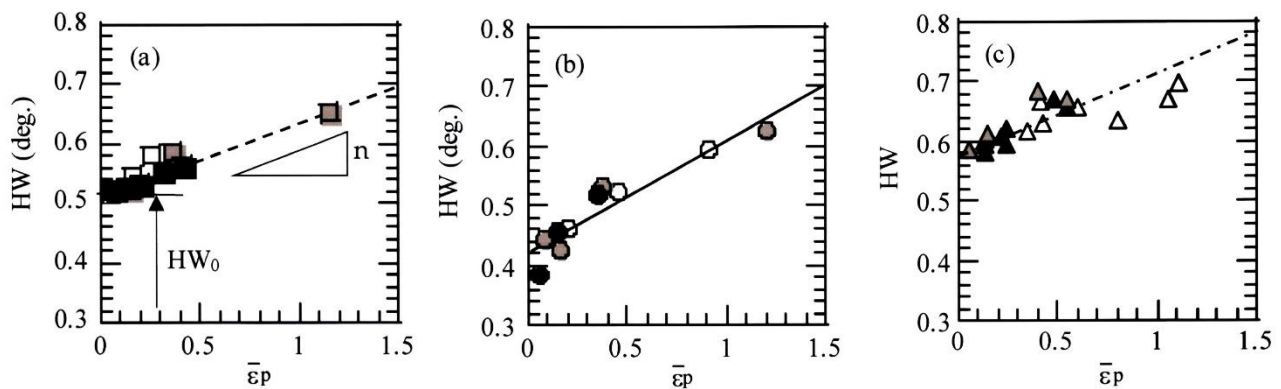


**Figure 4.** Relationships between X-ray half-width (HW) and equivalent plastic strain ( $\bar{\epsilon}_p$ ) in (a) TPF (square marks), (b) TAM (circle marks), and (c) TBF (triangle marks) steels. Open marks: in tension, solid black marks; in torsion, solid gray marks: in compression [39].

Tensile tests were conducted on a tensile testing machine (AD-10TD, Shimadzu Co., Kyoto, Japan) at 25 °C and with a mean strain rate of  $2.8 \times 10^{-3} \text{ s}^{-1}$  (crosshead speed: 10 mm/min). Three tensile specimens were used each to obtain the average tensile properties. Shear-punching was carried out at 25 °C and at a punching rate of 10 mm/min, with a shearing clearance between the die and punch of 10%. The diameter of the shear-punched hole was 4.76 mm. The dimensions of the die set made from JIS-SKD61 hot die steel are shown in Figure 2b. Three shear-punched holes were produced using shear-punching thin specimens to obtain the average shear-punching properties.

### 3. Results

#### 3.1. Microstructural and Tensile Properties

Figure 5 shows the SEM-EBSD images of the microstructures of three kinds of steel. The microstructure of TPF steel consists of a polygonal ferrite matrix structure and a mixed second phase of bainitic ferrite (carbide-free bainite) and retained austenite [6]. Some parts of the retained austenite exist in isolation. The original volume fraction, original carbon concentration, and  $k$ -value of retained austenite are  $f_{\gamma_0} = 8.0 \text{ vol\%}$ ,  $C_{\gamma_0} = 0.51 \text{ mass\%}$ , and  $k = 3.38$ , respectively (Table 2). The  $k$ -value is the strain-induced transformation factor or “mechanical stability” defined by the following equation [21],

$$k = (\ln f_{\gamma_0} - \ln f_\gamma) / \bar{\epsilon}_p \quad (1)$$

where  $f_{\gamma}$  is the volume fraction after being deformed to  $\bar{\epsilon}_p$ . In this research, the  $k$ -value was calculated in an equivalent plastic strain range between  $\bar{\epsilon}_p = 0$  and 0.3. Most of the retained austenite exists along the polygonal ferrite grain boundary and coexists with the bainitic ferrite phase.

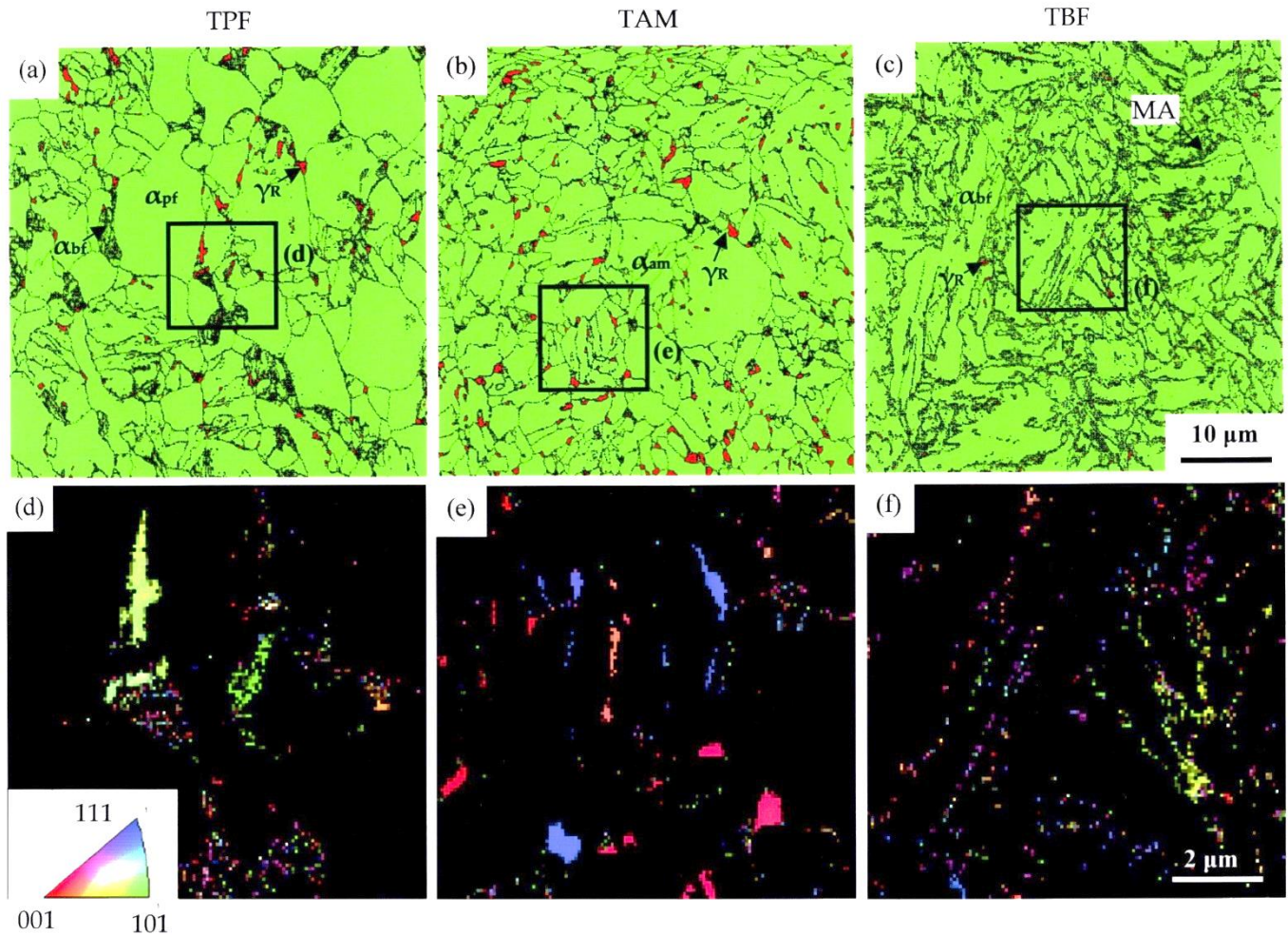


**Figure 5.** (a–c) Phase maps of BCC and FCC and (d–f) orientation maps of FCC in TPF, TAM, and TBF steels; (d–f) are high magnification of squares in (a–c).  $\alpha_{pf}$ ,  $\alpha_{am}$ ,  $\alpha_{bf}$ ,  $\gamma_R$ , and MA are polygonal ferrite, annealed martensite, bainitic ferrite (carbide-free bainite), retained austenite, and martensite–austenite mixed phase, respectively.

**Table 2.** Microstructural and mechanical properties of TPF, TAM, and TBF steels.

Steel	$f_{\gamma_0}$ (vol%)	$C_{\gamma_0}$ (mass%)	$k$	$f_{MA}$ (vol%)	HV <sub>0</sub>	YS (MPa)	TS (MPa)	UEI (%)	TEI (%)	RA (%)
TPF	$8.0 \pm 0.6$	$0.51 \pm 0.08$	3.38	0	329	762	1098	7.3	11.6	26.6
TAM	$12.4 \pm 0.4$	$0.84 \pm 0.06$	4.96	0	287	608	885	11.3	19.0	52.9
TBF	$11.4 \pm 1.2$	$0.65 \pm 0.14$	1.21	$2.0 \pm 0.3$	350	709	1276	9.0	17.7	49.5

$f_{\gamma_0}$ : retained austenite fraction,  $C_{\gamma_0}$ : carbon concentration of retained austenite,  $k$ : strain-induced transformation factor in an equivalent plastic strain range between  $\bar{\epsilon}_p = 0$  and 0.3,  $f_{MA}$ : volume fraction of MA phase, HV<sub>0</sub>: original Vickers hardness, YS: tensile yield stress, TS: tensile strength, UEI: uniform elongation, TEI: total elongation, RA: reduction in area.

The microstructure of TAM steel is composed of an annealed martensite (or tempered martensite) matrix structure and an isolated retained austenite on annealed martensite lath boundary [17,21]. Many retained austenite phases are isolated on the annealed martensite lath boundary. Such a microstructure is similar to duplex-type medium Mn steel [36]. The

original volume fraction, original carbon concentration, and  $k$ -value of retained austenite are  $f_{\gamma_0} = 12.4$  vol%,  $C_{\gamma_0} = 0.84$  mass%, and  $k = 4.96$ , respectively (Table 2). They are higher than those of TPF steel.

The microstructure of TBF steel consists of a bainitic ferrite matrix structure and refined retained austenite [27]. A high amount of retained austenite exists on the bainitic ferrite lath boundary. Notably, the retained austenite phases are much finer than those of the TPF and TAM steels. The original volume fraction, original carbon concentration, and  $k$ -value of retained austenite are  $f_{\gamma_0} = 11.4$  vol%,  $C_{\gamma_0} = 0.65$  mass%, and  $k = 1.21$ , respectively (Table 2). The volume fraction and carbon concentration are between TPF and TAM steels. The  $k$ -value is the smallest (or the mechanical stability of retained austenite is the highest) because of the refined retained austenite, although the carbon concentration of retained austenite is lower than that of TAM steel. Only TBF steel contains a small amount of MA phase (2.0 vol%).

Figure 6a shows the tensile engineering stress–strain ( $\sigma$ – $\epsilon$ ) curves of TPF, TAM, and TBF steels. The tensile properties are shown in Table 2. TAM steel has the lowest yield stress (YS) and tensile strength (TS), as well as the largest uniform elongation (UEL), total elongation (TEL), and reduction in area (RA). TBF steel has the highest tensile strength and original Vickers hardness ( $HV_0$ ). In addition, TBF steel has larger ductility (elongations and reduction in area) than TPF steel, although the ductility is lower than that of TAM steel. TPF steel has the highest yield stress and tensile strength between TAM and TBF steels, with small elongations and a minor reduction in area. Notably, TBF and TAM steels have large strain-hardening in an early strain range and a large strain range, respectively.

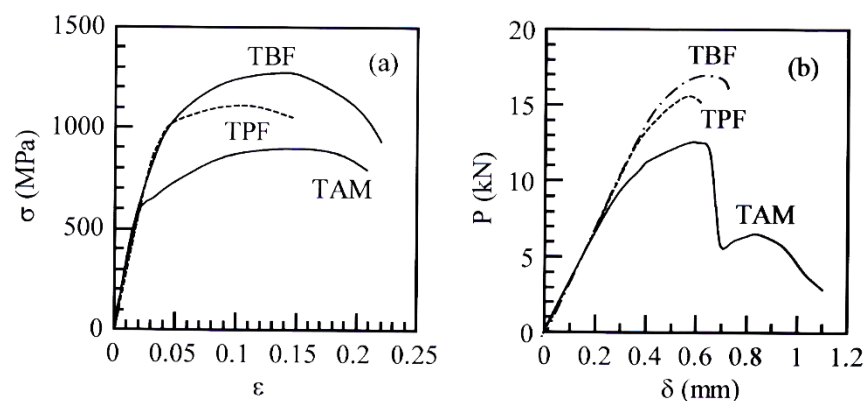


**Figure 6.** (a) Tensile engineering stress–strain ( $\sigma$ – $\epsilon$ ) curves [39] and (b) shear-punching load–stroke ( $P$ – $\delta$ ) curves of TPF, TAM, and TBF steels.

### 3.2. Shear-Punching Properties

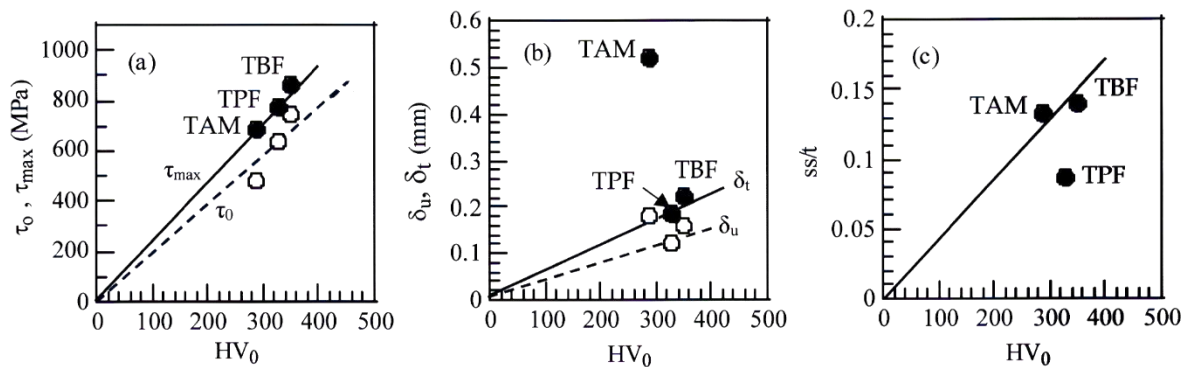
Figure 6b shows the typical shear-punching load–stroke ( $P$ – $\delta$ ) curves of TPF, TAM, and TBF steels. When the curves are compared to the  $\sigma$ – $\epsilon$  curves (Figure 6a), the  $P$ – $\delta$  curves exhibit a similar tendency to the  $\sigma$ – $\epsilon$  curves. It is noteworthy that only the  $P$ – $\delta$  curve of TAM steel shows a two-step curve.

Figure 7 shows the appearance of shear-punched surfaces in TPF, TAM, and TBF steels. These punched surfaces consist of a round portion (rp), a shear section (ss), and a break section (bs). The round portion lengths are negligible in TPF, TAM, and TBF steels. Notably, only the break section of TAM steel consists of the primary and the secondary shears relating to the two-step  $P$ – $\delta$  curve (Figure 6b). The break sections of TPF and TBF steels contain only the primary shear.



**Figure 7.** SEM micrographs of shear-punched surface in (a) TPF, (b) TAM, and (c) TBF steels. ss: shear section, bs: break section.

Figure 8 shows the variations in yield shear stress or 0.2% offset proof shear stress ( $\tau_0$ ), maximum shear stress ( $\tau_{\max}$ ), uniform shear displacement ( $\delta_u$ ), total shear displacement ( $\delta_t$ ), and a ratio of shear section length to sheet thickness ( $ss/t$ ) as a function of an original Vickers hardness ( $HV_0$ , Table 2) in shear-punched TPF, TAM, and TBF steels. These shear-punching properties, defined in Figure 2c, linearly increase with increasing  $HV_0$ . TBF steel has higher  $\tau_0$  and  $\tau_{\max}$  than TPF and TAM steels (Figure 8a). As shown in Figure 8b, TAM and TBF steels have higher  $\delta_u$  and  $\delta_t$  than those of TPF steel. It is noteworthy that the  $ss/t$  value of TPF is much lower than those of TAM and TBF steels.



**Figure 8.** Variations in (a) yield shear stress or 0.2% offset proof shear stress ( $\tau_0$ ) and maximum shear stress ( $\tau_{\max}$ ), (b) uniform shear displacement ( $\delta_u$ ) and total shear displacement ( $\delta_t$ ), and (c) a ratio of shear section length to thickness ( $ss/t$ ) as a function of original Vickers hardness ( $HV_0$ ) in TPF, TAM, and TBF steels.

### 3.3. Vickers Hardness Distribution and Equivalent Plastic Strain Distribution

Figure 9 shows the Vickers hardness (HV) distribution in the depth direction (X-direction, see Figure 10b) at the shear and break sections in the shear-punched surface layer of TPF, TAM, and TBF steels. If a Vickers hardness increment is defined by  $\Delta HV (=HV - HV_0, HV_0$ : original HV), the  $\Delta HV$  at the shear section of TPF steel is larger than that at the break section. In TAM steel, the opposite trend is seen. On the other hand, the  $\Delta HV$  at the break section of TBF steel is nearly the same as that at the shear section. When the  $\Delta HV$  values of these steels are compared, higher  $\Delta HV$ s are obtained at the break sections of TAM and TBF steels. If a critical depth fitting with  $\Delta HV = 0$  is defined by “ $d_h$ ” (Figure 9b,c), the  $d_h$  is about 300  $\mu m$  in TAM and TBF steels. In TPF steels, the  $d_h$  cannot be measured in a depth range lower than 400  $\mu m$ . TBF steel has the maximum HV near the surface. TPF steel exhibits the next maximum HV near the surface. TAM steel has lower maximum HV than TPF and TBF steels, except for the unusually high HV due to secondary shear (see arrows in Figure 9b).

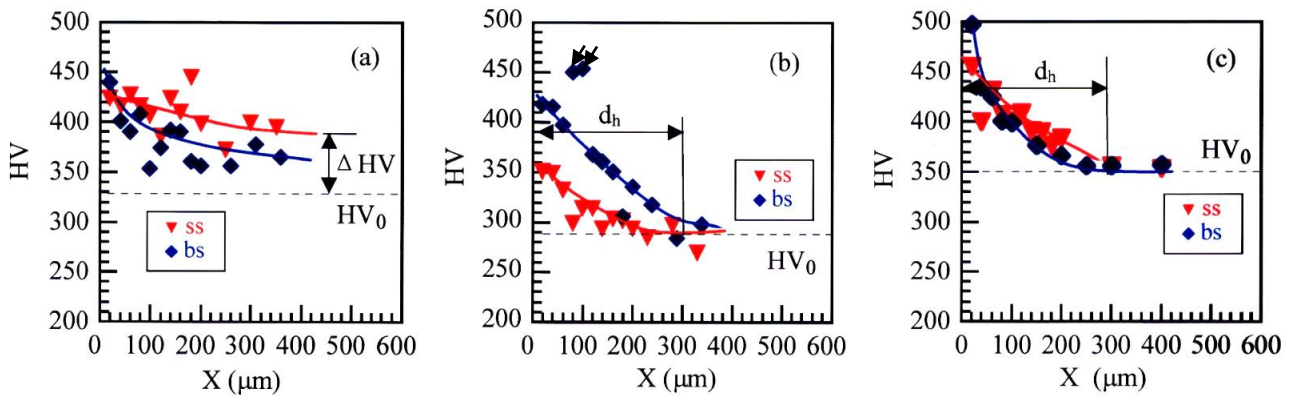


**Figure 9.** Vickers hardness distribution (HV) in the depth direction (X-direction) at the shear section (ss) and break section (bs) in (a) TPF, (b) TAM, and (c) TBF steels. The arrows in (b) are unusual Vickers hardness.  $\Delta HV$  is Vicker hardness increment ( $=HV - HV_0$ ). Additionally, “ $d_h$ ” is a critical depth fitting with  $\Delta HV = 0$ .

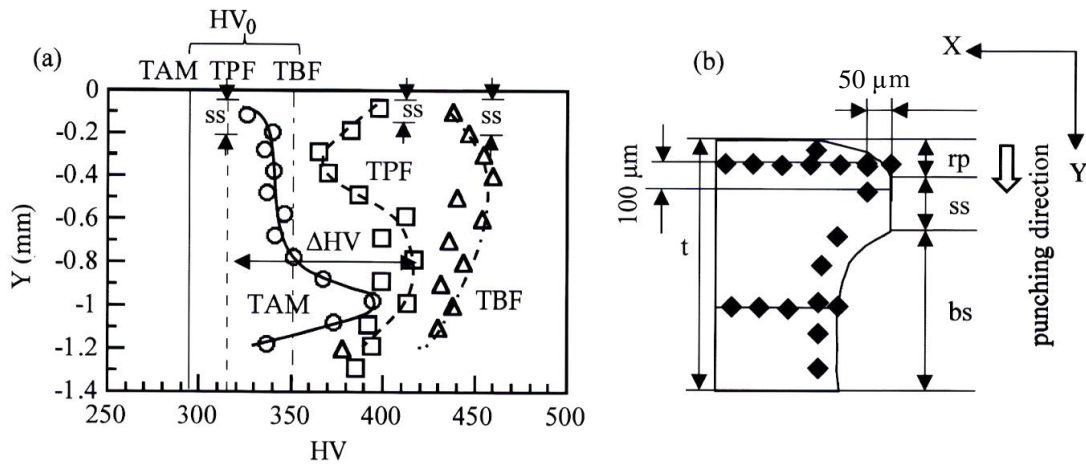


**Figure 10.** (a) Vickers hardness (HV) distribution in the thickness direction (Y-direction) in the shear-punched surface layer of TPF, TAM, and TBF steels; (b) directions and spots of Vickers hardness measurement.  $t$ : sheet thickness,  $rp$ : round portion length,  $ss$ : shear section length,  $bs$ : break section length.

Figure 10a shows the HV distribution in the punching direction (Y-direction) in the shear-punched surface layer of TPF, TAM, and TBF steels. The HV is measured inside  $50 \mu\text{m}$  from the surface (see Figure 10b). The maximum HV is obtained at the break section in all steels, although the HV at the shear section of TPF steel is relatively high. The  $\Delta HV$ s at the break section of TBF steel are larger than those of TPF and TAM steel. Notably, the HV and  $\Delta HV$  at the shear section of TAM steel are much lower than those at the break section, differing from those of TPF and TBF steels.

Figure 11 shows the  $\bar{\epsilon}_p$  distribution in the depth direction (X-direction) at the shear and break sections in the shear-punched surface layer of TPF, TAM, and TBF steels. In TPF steel, the  $\bar{\epsilon}_p$  rapidly decreases with increasing depth in a range of  $X = 0$  to  $50 \mu\text{m}$ . On the other hand, the  $\bar{\epsilon}_p$  of TAM steel gradually decreases with increasing depth in a range of  $X = 0$  to  $500 \mu\text{m}$ , although the maximum  $\bar{\epsilon}_p (=1.9)$  is lower than those of TPF and TBF steels. The  $\bar{\epsilon}_p$  distribution of TBF steel shows an intermediate tendency between TPF and TAM steels, with the largest maximum  $\bar{\epsilon}_p (=3.3)$ . The difference in  $\bar{\epsilon}_p$  between the shear and break sections in TAM steel is larger than those of TPF and TBF steels. This may result in a large difference in HV (Figure 9b).

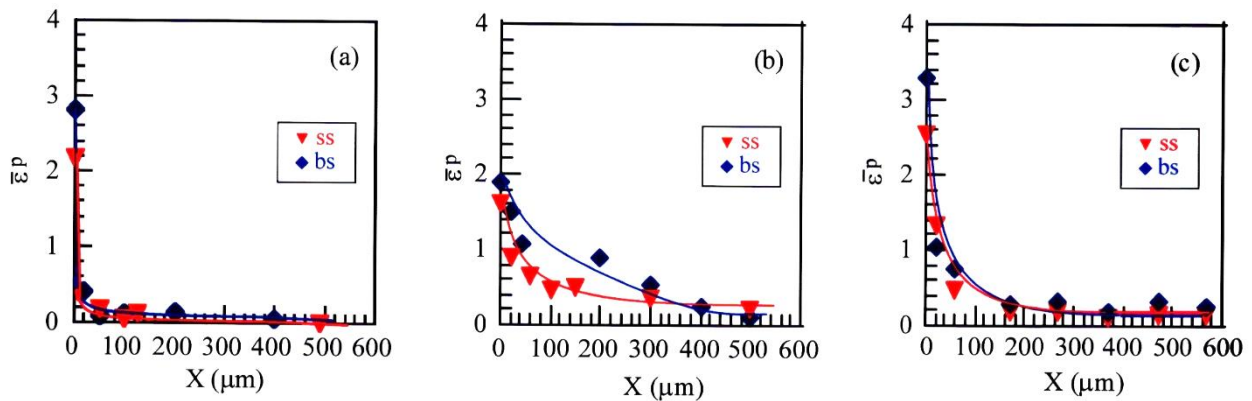


**Figure 11.** Equivalent plastic strain ( $\bar{\epsilon}_p$ ) distribution in the depth direction (X-direction) at the shear section (ss) and break section (bs) in the shear-punched surface layer of (a) TPF, (b) TAM, and (c) TBF steels.

### 3.4. Strain-Induced Martensite Fraction Distribution

Figure 12 shows the variations in the retained austenite fraction in the depth direction (X-direction) at the shear and break sections in the shear-punched surface layer of TPF, TAM, and TBF steels. A larger amount of retained austenite transforms to martensite at TAM steel's shear and break sections. The strain-induced martensite fraction ( $\Delta f_{\alpha_m} = f_{\gamma_0} - f_{\gamma}$ ) becomes the maximum on the punched surface and decreases with increasing depth in all steels.

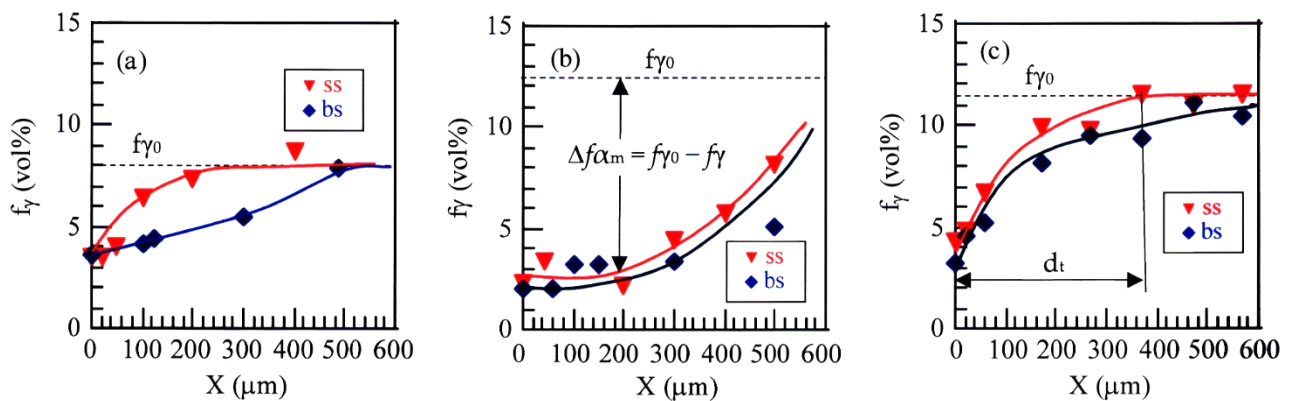


**Figure 12.** Retained austenite distribution in the depth direction (X-direction) at the shear section (ss) and break section (bs) in the shear-punched surface layer of (a) TPF, (b) TAM, and (c) TBF steels.  $\Delta f_{\alpha_m}$  is the strain-induced martensite fraction. Additionally, “ $d_t$ ” is a critical depth of non-transformation.

The  $\Delta f_{\alpha_m}$  at the break section is higher than that at the shear section in all steels. In TPF and TBF steels, the  $\Delta f_{\alpha_m}$  rapidly decreases with increasing depth, in contrast to TAM steel, except for the  $\Delta f_{\alpha_m}$  at the break section of TPF steel. The critical depths of non-transformation “ $d_t$ ” at the shear section are about 300  $\mu\text{m}$  and 400  $\mu\text{m}$  in TPF and TBF steels, respectively. In this case, the  $d_t$ s of the break section are higher than those at the shear section in TPF and TBF steels. On the other hand, the  $d_t$ s at the shear and break sections are higher than 600  $\mu\text{m}$  in TAM steel.

### 3.5. Initiated Micro-Crack/Void Characteristics

Figure 13 shows the SEM images of the cross-section of the shear-punched surface layer in TPF, TAM, and TBF steels. First, the micro-crack/void initiation sites are explained. Most of the micro-crack/void in TPF steel seems to initiate at the interface between polygonal ferrite and the second phase, as seen with bainitic ferrite, retained austenite, and strain-induced martensite (Figure 13d). In the same way as TPF steel, many micro-

cracks/voids also initiate at the matrix structure/second phase interface in TAM and TBF steels (Figure 13h,l). Barnwal et al. [20] reported that micro-void initiation sites are the interface between the polygonal ferrite and the second phase at the break section in 980 MPa grade TPF steel. Sugimoto et al. showed the same micro-void initiation sites in 0.1–0.6C–1.5Si–1.5Mn TAM [21] and TBF steels [21,27]. Also, Tan et al. [31] showed that tiny cracks are observed among the fine bainite region with film-like MA phase in 0.20C–1.40Si–1.70Mn–0.045Nb CFB steels. The present micro-crack/void initiation sites show the same tendency as their reports. Micro-void initiation at the matrix/the second phase interface is also reported in Q and P [29], duplex-type MMn [36], and TM [26] steels, although a grain boundary crack initiates in TWIP steel [24].

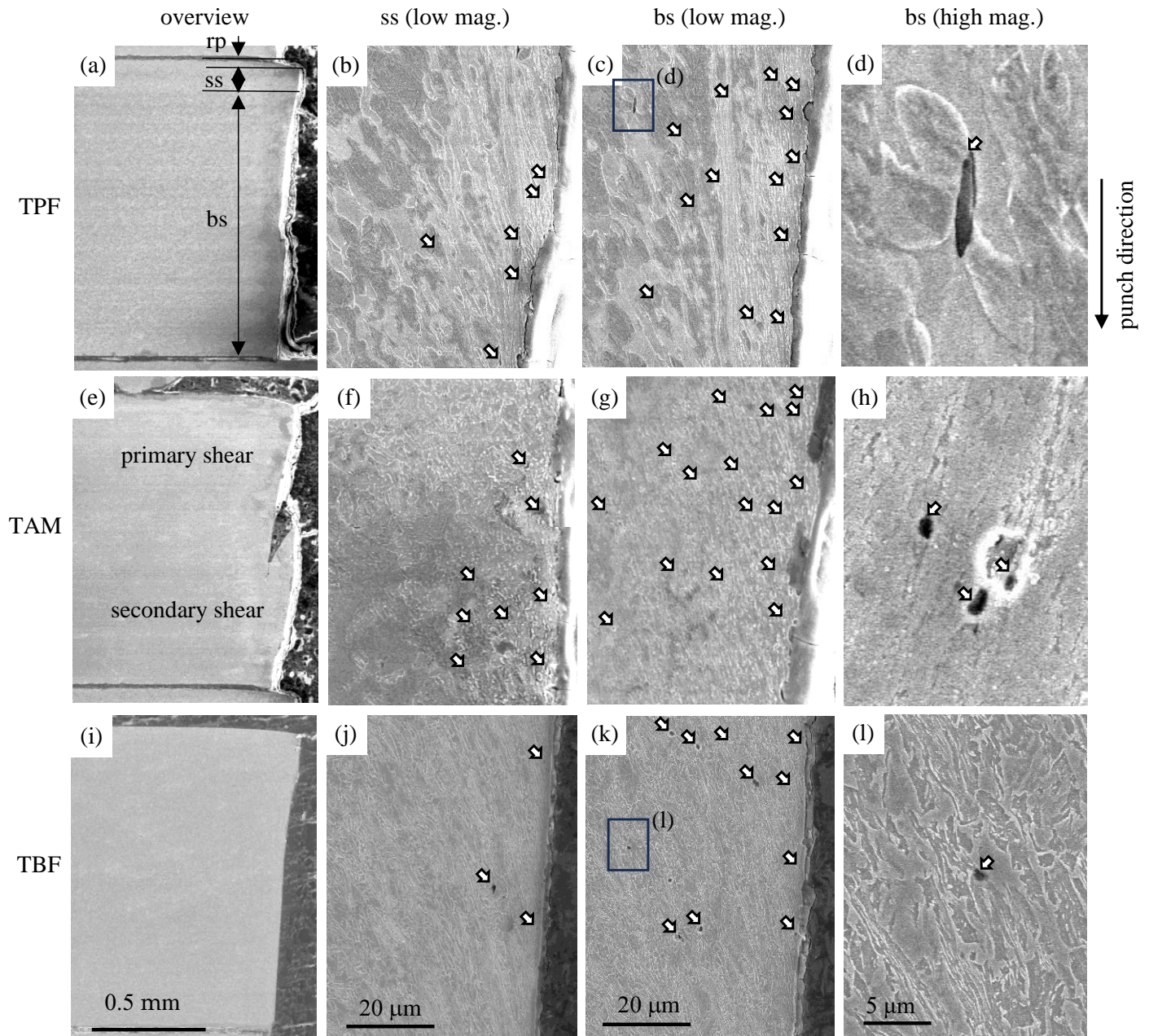


**Figure 13.** SEM images of (a,e,i) overview, (b,f,j) low magnification at the shear section, and (c,g,k) low magnification at the break section of the cross-section of the shear-punched surface layer in TPF, TAM, and TBF steels. (d,h,l) High magnification at the break section subjected to the equivalent plastic strain of  $\bar{\epsilon}_p = 0.3$ . (d) and (l) are high magnification of squares in (c) and (k), respectively. Arrows denote micro-crack/void. Notably, rp: round portion, ss: shear section, bs: break section.

Next, we shall state the mean size ( $D_v$ ) and the mean number ( $N_v$ ) of the micro-crack/void. A larger number of micro-cracks/voids initiate at the break section in all steels, compared to the shear section. In a depth range of  $X = 0$  to  $50 \mu\text{m}$  (on the outmost surface), TAM steel contains a larger number of micro-cracks/voids than those of TPF and TBF steels (Figure 13c,g,k), in addition to a much larger equivalent plastic strain. The mean number of micro-cracks/voids of TBF steel is the smallest. If the numbers of micro-cracks/voids of the present TPF, TAM, and TBF steels were compared to those of other AHSSs, a larger number of micro-cracks/voids ( $N_v = 1.35 \times 10^4/\text{mm}^2$ ) initiated only in duplex-type MMn steel (0.20C-1.50Si-4.94Mn with retained austenite of  $f\gamma_0 = 39.4 \text{ vol}\%$ ) [36].

To compare quantitatively the micro-void initiation behavior in the shear-punched surface layer with that in the steels deformed to  $\bar{\epsilon}_p = 0.3$  in tension, torsion, and compression, the  $D_v$  and  $N_v$  at the shear and break sections subjected to  $\bar{\epsilon}_p = 0.3$  were measured in TPF, TAM, and TBF steels (Figure 14). In this case, the depths at which an equivalent plastic strain reaches  $\bar{\epsilon}_p = 0.3$  at the break section are about  $X = 20, 400,$  and  $200 \mu\text{m}$  in TPF, TAM, and TBF steels, respectively (Figure 11). The mean sizes ( $D_v = 1.5$  to  $2 \mu\text{m}$ ) are larger than those ( $D_v = 1 \mu\text{m}$ ) of TAM and TBF steels (Figure 14a). As shown in Figure 14b, a larger number of voids initiate at the shear and break sections in TPF steel compared to TAM and TBF steels. It is noteworthy that the mean number of micro-cracks/voids is significantly small at the shear and break sections in TBF steel.

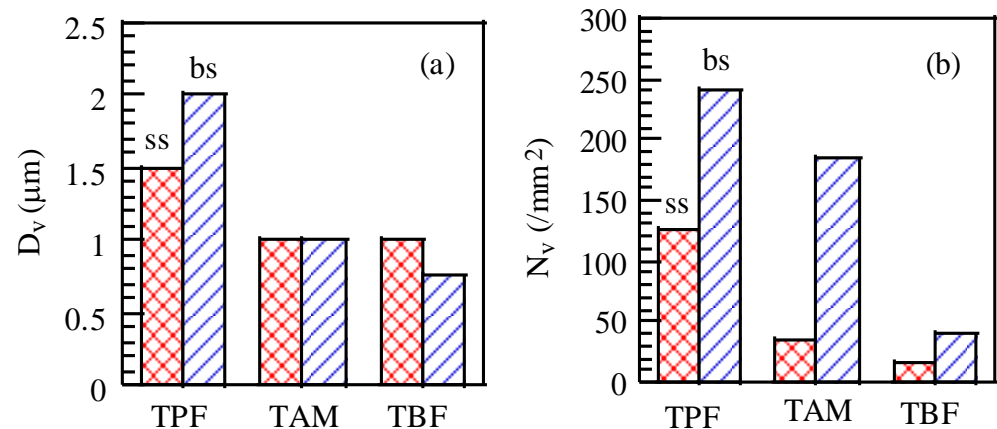


**Figure 14.** Variations in (a) the mean size ( $D_v$ ) and (b) the mean number of ( $N_v$ ) of micro-crack/void at the shear section (ss) and break section (bs) in TAM, TPF, and TBF steels, which were measured at the depth subjected to the equivalent plastic strain of  $\bar{\epsilon}_p = 0.3$ .

#### 4. Discussion

The typical stress distribution of the shear region subjected to shear-punching is shown in Figure 15 [38], and it is mainly negative mean normal stress including zero one, except for a part of the positive mean normal. In the following, the damage properties of the shear-punched surface layer are related to the mean normal stress using the data of the strain hardening, the strain-induced martensite transformation, and the micro-crack/void initiation behaviors on deforming in tension, torsion, and compression [39]. Additionally, the effect of microstructural properties on the surface layer damage is discussed. Furthermore, the relationship between the stretch-flangeability and the surface layer damage is discussed.

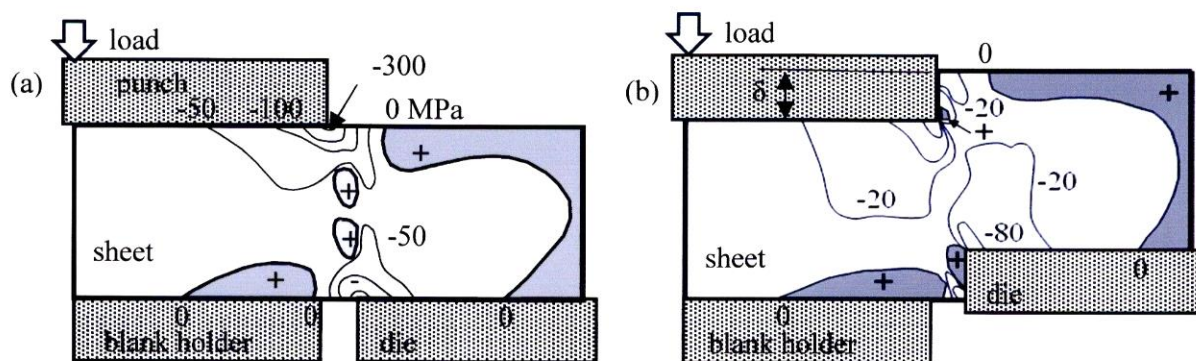


**Figure 15.** Mean normal stress distribution on shear-punching [38]. (a) shear-punching stroke  $\delta = 0$  to 3.76% of sheet thickness, (b)  $\delta = 25\%$  of sheet thickness. Shearing clearance between punch and die: 10% of sheet thickness. Material: JIS-A1100. This figure is redrawn with permission from The Japan Society for Technology of Plasticity, copyright 2024.

#### 4.1. Strain-Induced Martensite Transformation Behavior

Figure 16 shows the variations in retained austenite fraction with increasing equivalent plastic strain at the shear and break sections of TPF, TAM, and TBF steels. When these retained austenite fractions were compared to those of steels deformed in tension, torsion, and compression [39], the retained austenite fraction at the shear and break sections was to the same extent as compressive and torsional deformations in TPF and TAM steels, although the former was higher than the latter in TBF steel. This indicates that the shear and break sections on shear-punching mainly deformed under negative mean normal stress, including zero one.

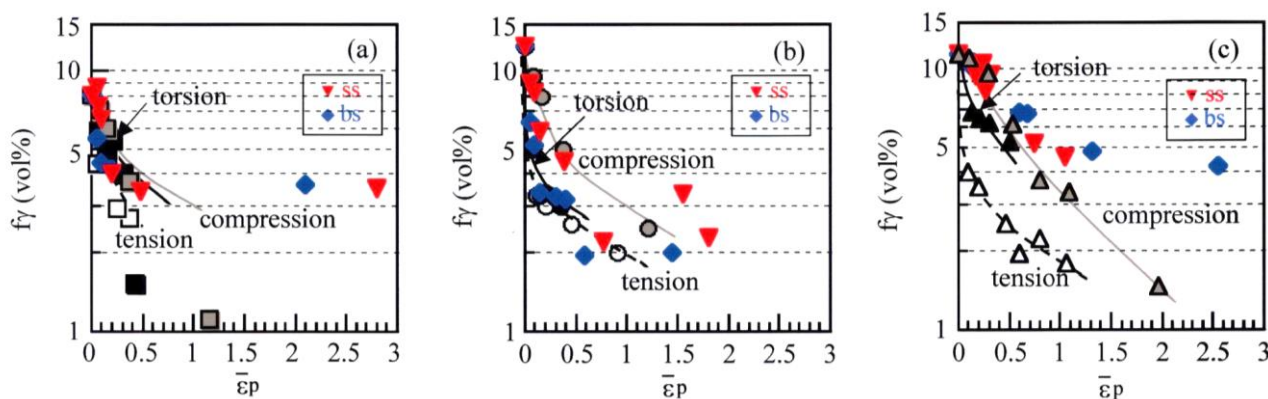


**Figure 16.** Variations in volume fraction of untransformed retained austenite ( $f_\gamma$ ) as a function of equivalent plastic strain ( $\bar{\epsilon}_p$ ) at the shear section (ss) and break section (bs) in (a) TPF, (b) TAM, and (c) TBF steels. Data in tension (open marks), torsion (solid black marks), and compression (solid gray marks) from Ref. [39] were redrawn. Square, circle, and triangle marks are data of TPF, TAM, and TBF steels, respectively.

In Figure 12b, the  $\Delta f_{\alpha_m}$  on the surface and inside at the break section were the largest in TAM steel, in addition to those at the shear section. This may be associated with a large amount of retained austenite with low mechanical stability (high  $k$ -value, Table 2) and a large equivalent strain at the break section (Figure 11b). The latter is responsible for the secondary shear (Figures 7b and 13e) and annealed martensite matrix structure with high ductility (Figure 5b). In TBF steel, the  $\Delta f_{\alpha_m}$  were lower than those of TAM steel (Figures 12 and 16). This is considered to be mainly associated with the higher mechanical stability (lower  $k$ -value) of fine-sized retained austenite (Table 2). The lowest  $\Delta f_{\alpha_m}$  at the break section of TPF steel may be caused by the lowest initial volume fraction of retained austenite and a small ratio of the shear section length to sheet thickness (Figure 8c).

#### 4.2. Strain-Hardening Behavior

As shown in Figures 9 and 10, a larger  $\Delta HV$  in the shear-punched surface layer was observed at the shear and break sections of TBF steel compared to TPF steel, although the  $\Delta HV$ s were nearly the same as the  $\Delta HV$  at the break section in TAM steel. According to Sugimoto et al. [21], the  $\Delta HV$  of the shear-punched surface layer in TRIP-aided steel is mainly controlled by the following hardenings (in the same way as tensile strain-hardening):

- (1) “Long-range internal stress hardening”, which results from the difference in plastic strain between matrix structure and the second phase (retained austenite, strain-induced martensite, MA phase, etc.) [45],
- (2) “Strain-induced martensite transformation hardening”, which results from an increase in strain-induced martensite fraction, although the transformation relaxes the localized stress concentration through an expansion strain [46],
- (3) “Forest dislocation hardening”, which is estimated by the Ashby equation [47].

As shown in Figure 6a, TBF steel exhibited a large strain-hardening rate in an early stage with the highest flow stress. Therefore, high  $\Delta HV$  in the shear and break sections of TBF steel may be caused by the large strain-hardening of the bainitic ferrite matrix structure and strain-induced martensite transformation hardening [39]. On the other hand, high  $\Delta HV$  at the break section of TAM steel is considered to be mainly associated with a significant strain-induced martensite transformation hardening (Figure 12b), as well as high long-range internal stress hardening resulting from soft annealed martensite matrix structure and carbon-enriched hard strain-induced martensite. An exceptionally large  $\Delta HV$  at the break section of TAM steel (Figures 9b and 10a) may be caused by the secondary shear (Figure 7b). Additionally, the secondary shear is considered to produce a large  $\bar{\epsilon}_p$  inside the shear-punched surface layer (Figure 11b), although the  $\bar{\epsilon}_p$  on the surface was smaller than those of TPF and TBF steels.

The critical hardening depth for  $\Delta HV$  was unclear in TPF steel (Figure 9a), although TAM and TBF steels had the critical depth of  $d_h = 300 \mu\text{m}$  (Figure 9b,c). Additionally, inner  $\Delta HV$  at the shear section was higher than that at the break section (Figure 9a), which was different from TAM and TBF steels. These reasons are in consideration. According to Sugimoto et al. [39], the strain-hardening behavior on an equivalent stress–strain curve does not significantly depend on the mean normal stress in TPF, TAM, and TBF steels; therefore, the effect of the mean normal stress on the HV distribution of Figure 9 can be neglected.

#### 4.3. Micro-Crack/Void Initiation Behavior

First, let us confirm the mean normal stress developed on shear-punching for the micro-crack/void formation behavior. Figure 17 shows the relationships between the  $N_v$  and  $D_v$  of micro-cracks/voids at the shear and break sections in TPF, TAM, and TBF steels. In this case, the relationship cannot be compared to that of compressive deformation because of no-void initiation. It is found that the relationships nearly agree with those of torsional deformation in all steels in nearly the same way as the mean normal stress on the strain-induced martensite transformation of Figure 16. Figure 18 compares the shear and break sections subjected to  $\bar{\epsilon}_p = 0.3$  with those deformed to  $\bar{\epsilon}_p = 0.3$  under the different mean normal stresses in TPF, TAM, and TBF steels. The  $D_v$  and  $N_v$  at the shear and break sections agree with those of the mean normal stress of 0 and 0 to  $-500 \text{ MPa}$ , respectively. This indicates that the  $D_v$  and  $N_v$  at the shear and break sections were deformed in torsion and compression in a similar way to Figure 15.

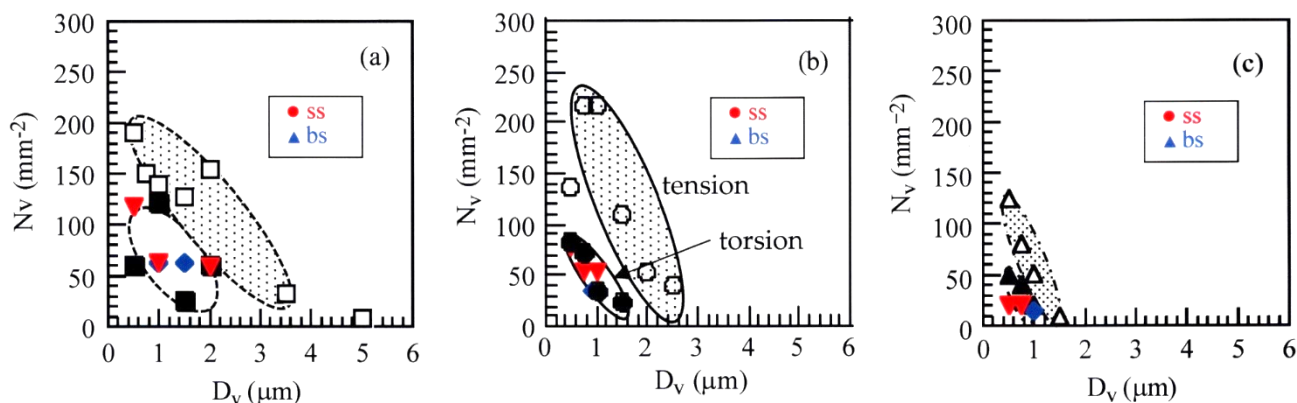


**Figure 17.** The relationship between the mean size of void ( $D_v$ ) and the mean number of void ( $N_v$ ) at the shear section (ss) and break section (bs) subjected to the equivalent plastic strain of  $\bar{\epsilon}_p = 0.3$  in (a) TPF (square marks), (b) TAM (circle marks), and (c) TBF (triangle marks) steels, which are compared to them deformed to  $\bar{\epsilon}_p = 0.3$  in torsion (solid black marks) and tension (open black marks). Data in torsion and tension were redrawn from Ref. [39].

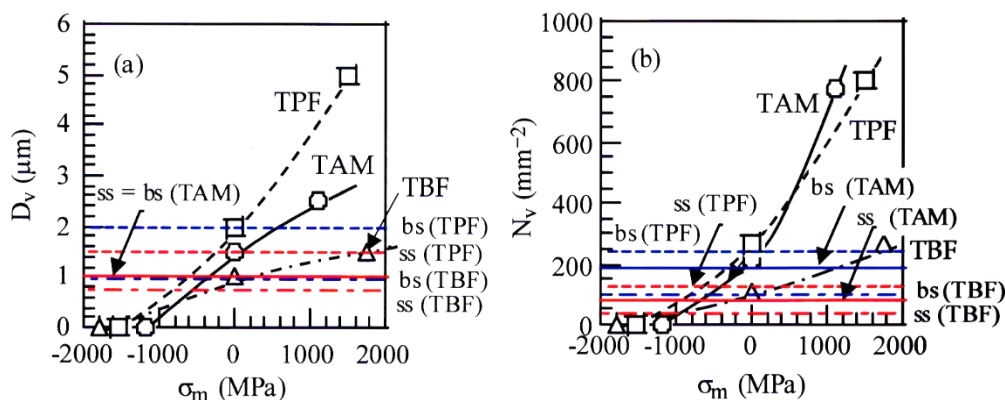


**Figure 18.** Comparison of (a) the mean size of void ( $D_v$ ) and (b) the mean number of void ( $N_v$ ) measured at the depth subjected to an equivalent plastic strain of  $\bar{\epsilon}_p = 0.3$  to them deformed in tension, torsion, and compression to  $\bar{\epsilon}_p = 0.3$  in TPF (square marks), TAM (circle marks), and TBF (triangle marks) steels.

Next, let us discuss the relationship between the micro-crack/void initiation behavior and the other shear-punched surface layer's damage properties, such as the  $\Delta HV$ ,  $\Delta f\alpha_m$ , and  $\bar{\epsilon}_p$ , as well as the  $ss/t$  value. In TBF steel, the  $\Delta HV$  rapidly decreased with increasing depth in a range from  $X = 0$  to  $300 \mu\text{m}$  (Figure 9c). The  $\bar{\epsilon}_p$  and  $\Delta f\alpha_m$  were intermediate between those of TAM and TPF steels (Figures 11 and 12). These results indicate that the suppressed micro-crack/void initiation behavior of TBF steel is related to the moderate  $\bar{\epsilon}_p$  and  $\Delta f\alpha_m$ . On the other hand, the micro-crack/void initiation behavior of TAM steel was characterized by the largest critical depth for micro-crack/void initiation and a small  $D_v$  (with relatively high  $N_v$ ) (Figure 14). In TAM steel, large  $\Delta HV$ ,  $\Delta f\alpha_m$ , and  $\bar{\epsilon}_p$  were produced inside at the break section, although the  $\bar{\epsilon}_p$  near the surface was the lowest (Figures 9, 11 and 12). Therefore, the large critical depth for micro-crack/void initiation of TAM steel may be mainly caused by the large  $\bar{\epsilon}_p$ . In this case, large  $\Delta f\alpha_m$  increases the number of the micro-crack/void initiation site by increasing the strength ratio of the strain-induced martensite to the matrix structure, although it also plays a role in suppressing the void initiation by lowering the localized stress concentration. A large  $ss/t$  value of TBF steel may also contribute to small surface layer damage in the same way as with TAM steel.

Finally, let us discuss the relationship between micro-crack/void initiation behavior and microstructural properties. Generally, micro-crack/void initiation in TRIP-aided steels is mainly controlled by microstructural properties such as the following (i) to (iii) [11,21,27]:

- (i) Refinement and homogeneity of the microstructure;
- (ii) Strength ratio of the second phase to the matrix structure;
- (iii) Volume fraction and mechanical stability of retained austenite.

The microstructure of TBF steel had a fine bainitic ferrite lath structure matrix with high homogeneity (Figure 5c), a small strength ratio of the strain-induced martensite to the matrix structure, and high mechanical stability of the retained austenite (Table 2). These microstructural properties are considered to effectively suppress the micro-crack/void initiation in TBF steel. In this case, the effect of the MA phase on the micro-crack/void initiation is expected to be neglected because of a small amount. In TAM steel, the micro-crack/void initiation at the shear and break sections was suppressed next to that of TBF steel (Figure 14). This is caused by the fine and low-hardness annealed martensite matrix structure with high ductility (Figure 5b), although a large  $\bar{\epsilon}_p$ , a large  $\Delta f\alpha_m$  through the low mechanical stability and a large amount of retained austenite, as well as a high strength ratio due to the hard strain-induced martensite, promoted the micro-crack/void initiation, particularly near the surface. In TPF steel, micro-crack/void initiation was promoted at the shear and break sections. This was caused by the coarse polygonal ferrite structure matrix, a small amount of retained austenite, and a high strength ratio, as well as a small  $ss/t$  value.

#### 4.4. Relationship between the Stretch-Flangeability and Shear-Punched Surface Layer Damage

In general, the stretch-flangeability of TRIP-aided steel is mainly controlled by the micro-crack/void initiation on shear-punching [14,17,21,22,26,29,35,36] and the following crack growth and/or void connection on hole-expanding [13,35], which are related to the matrix structure, the retained austenite characteristics, and the  $ss/t$  value. As shown in Figure 1b, TBF steel had excellent stretch-flangeability compared to TPF and TAM steels, displaying high stretch-formability (Figure 1a). In TBF steel, the micro-crack/void initiation on shear-punching was considerably suppressed in the shear-punched surface layer (Figures 13 and 14), although large strain-hardening occurred (Figure 9c). Therefore, the excellent stretch-flangeability of TBF steel may be mainly associated with the suppressed micro-crack/void initiation behavior on shear-punching and high crack propagation and/or void connection resistance on hole-expanding [48] resulting from the fine bainitic ferrite lath matrix structure (Figure 5c), a small strength ratio, and high mechanical stability of retained austenite (Table 2 and Figure 16c). In this case, the strain-induced transformation of the untransformed retained austenite plays a role in suppressing the crack growth and/or void connection on hole expansion through the plastic relaxation of localized stress.

TAM steel had higher stretch-flangeability than TPF steel, although the stretch-flangeability was lower than that of TBF steel (Figure 1b). In TAM steel, the micro-crack/void initiation on shear-punching was suppressed compared to that of TPF steel (Figure 14), although a larger number of micro-crack/voids were initiated on the outmost surface in comparison to TPF steel. In addition, a larger amount of retained austenite transformed to martensite (Figure 12b) and a larger equivalent plastic strain developed in the shear-punched surface layer (Figure 11b). The former increases the strength ratio. Therefore, the relatively high stretch-flangeability of TAM steel is considered to be associated with small-size micro-crack/void initiation on shear-punching and high crack growth and/or void connection resistance on hole-expanding resulting from a fine annealed martensite lath structure matrix with high ductility, with a contribution of a large amount of inner untransformed retained austenite, in a similar way to TBF steel.

## 5. Conclusions

The damage properties of the shear-punched surface layer, such as the strain-hardening increment, strain-induced martensite fraction, and initiated micro-crack/void characteristics at the shear and break sections, were experimentally investigated to relate to the stretch-flangeability in low-carbon TPF, TAM, and TBF steels with different matrix struc-

tures. In addition, the surface layer's damage properties were related to the mean normal stress that develop on shear-punching and microstructural properties. The main results are summarized as follows:

1. The shear-punched surface damage of these steels was experimentally confirmed to be produced under the mean normal stress of negative to 0 MPa (from compressive to torsional deformation).
2. The surface layer damage of TBF steel was distinguished by considerably suppressed micro-crack/void initiation with a large hardness increment and moderate strain-induced martensite transformation. The suppressed micro-crack/void initiation was associated with the fine bainitic ferrite lath matrix structure, a small strength ratio, and the high mechanical stability of retained austenite.
3. The surface layer damage of TAM steel was characterized by a large plastic strain (hardness increment) and a large amount of strain-induced martensite transformation. However, micro-crack/void initiation was suppressed next to TBF steel and the critical depth for no-void initiation was the maximum. This is caused by the fine annealed martensite structure matrix structure with high ductility and a large amount of retained austenite, despite the low mechanical stability of retained austenite and the high strength ratio developed by carbon-enriched strain-induced martensite.
4. The shear-punched surface layer damage at the break section of TPF steel was mainly characterized by the easiest micro-crack/void initiation, with an equivalent small plastic strain and a small amount of strain-induced martensite transformation. This was caused by the coarse polygonal ferrite structure matrix, a small amount of retained austenite, and a high strength ratio, as well as a small  $ss/t$  value.
5. The excellent stretch-flangeability of TBF steel might be caused by the considerably suppressed micro-crack/void initiation on shear-punching and the high crack propagation/void connection resistance on hole-expanding resulting from a fine bainitic ferrite matrix structure and a large amount of mechanically stable retained austenite.
6. On the other hand, the next high stretch-flangeability of TAM steel was considered to be mainly associated with a small-sized micro-crack/void initiation on shear-punching and high crack growth/void connection resistance resulting from a fine annealed martensite lath structure matrix with high ductility, with a contribution of a large amount of inner untransformed retained austenite.

**Author Contributions:** Author Contributions: Conceptualization, K.-i.S.; methodology, K.-i.S. and S.S.; formal analysis, K.-i.S. and S.S.; investigation, S.S. and J.K.; resources, K.-i.S.; data curation, K.-i.S., S.S. and J.K.; writing—original draft preparation, S.S.; writing—review and editing, K.-i.S.; visualization, S.S.; supervision, K.-i.S. and J.K. All authors have read and agreed to the published version of the manuscript.

**Funding:** This research received no external funding.

**Institutional Review Board Statement:** Not applicable.

**Informed Consent Statement:** Not applicable.

**Data Availability Statement:** The original contributions presented in the study are included in the article, further inquiries can be directed to the corresponding author.

**Conflicts of Interest:** The author declares no conflicts of interest.

## References

1. Senuma, T. Physical metallurgy of modern high strength steel sheets. *ISIJ Int.* **2001**, *42*, 520–532. [[CrossRef](#)]
2. Bouaziz, O.; Zurob, H.; Huang, M. Driving force and logic of development of advanced high strength steels for automotive applications. *Steel Res. Int.* **2013**, *84*, 937–947. [[CrossRef](#)]
3. Rana, R.; Singh, S.B. *Automotive Steels—Design, Metallurgy, Processing and Applications*; Woodhead Publishing: Cambridge, UK, 2016; pp. 1–469.
4. Bleck, W.; Guo, X.; Ma, Y. The TRIP effect and its application in cold formable sheet steel. *Steel Res. Int.* **2017**, *88*, 1700218. [[CrossRef](#)]

5. Krizan, D.; Steineder, K.; Kaar, S.; Hebesberger, T. Development of third generation advanced high strength steels for automotive applications. In Proceedings of the 19th International Scientific Conference Transfer 2018, Trencin, Slovakia, 22–23 November 2018; pp. 1–15.
6. Soleimani, M.; Kalthor, A.; Mirzadeh, H. Transformation-induced plasticity (TRIP) in advanced steels: A review. *Mater. Sci. Eng. A* **2020**, *795*, 140023. [[CrossRef](#)]
7. Zurnadzhy, V.I.; Efremenko, V.G.; Petryshynets, I.; Chabak, Y.G.; Efremenko, A.V. *Improvement of Mechanical Properties of Structural Steels by Multi-Phase Structure Formation*; Premier Publishing: Praha, Czech Republic, 2022; pp. 1–142.
8. Hasegawa, K.; Kawamura, K.; Urabe, T.; Hosoya, Y. Effects of microstructure on stretch-flange-formability of 980 MPa grade cold-rolled ultra high strength steel sheets. *ISIJ Int.* **2004**, *44*, 603–609. [[CrossRef](#)]
9. Shoji, H.; Hino, K.; Ohta, M.; Shinohara, Y.; Minami, F. Ductile fracture mechanism for dual phase steel with high strength second phase. *Trans. Jpn. Weld. Soc.* **2015**, *33*, 341–348. (In Japanese) [[CrossRef](#)]
10. Fan, D.; Fonstein, N.; Jun, H. Effect of microstructure on tensile properties and cut-edge formability of DP, TRIP, Q&T and Q&P steels. *AIST Trans.* **2016**, *13*, 180–185.
11. Takashima, K.; Hasegawa, K.; Toji, Y.; Funakawa, Y. Void generation in cold-rolled dual-phase steel sheet having excellent stretch flange formability. *ISIJ Int.* **2017**, *57*, 1289–1294. [[CrossRef](#)]
12. Heibel, S.; Dettinger, T.; Nester, W.; Clausmeyer, T.; Tekkaya, A.E. Damage mechanism and mechanical properties of high-strength multiphase steels. *Materials* **2018**, *11*, 761. [[CrossRef](#)]
13. Song, E.; Lee, G.; Jeon, H.; Park, B.; Lee, J.; Kim, J. Stretch-flangeability correlated with hardness distribution and strain-hardening of constituent phases in dual- and complex-phase steels. *Mater. Sci. Eng. A* **2021**, *817*, 141353. [[CrossRef](#)]
14. Han, S.; Chan, Y.; Wang, C.Y.; Dong, H. A comprehensive investigation on the damage induced by the shearing process in DP780 steel. *J. Mater. Process. Tech.* **2022**, *299*, 117377. [[CrossRef](#)]
15. Matsumura, O.; Sakuma, Y.; Ishii, Y.; Zhao, J. Effect of retained austenite on formability of high strength sheet steels. *ISIJ Int. C.* [[CrossRef](#)]
16. Hiwatashi, S.; Takahashi, M.; Katayama, T.; Usuda, M. Effect of deformation-induced transformation on deep drawability—Forming mechanism of TRIP type high-strength steel sheet. *J. Jpn. Soc. Technol. Plast.* **1994**, *35*, 1109–1114. (In Japanese)
17. Sugimoto, K.; Kobayashi, M.; Nagasaka, A.; Hashimoto, S. Warm stretch-formability of TRIP-aided dual-phase sheet steels. *ISIJ Int.* **1995**, *35*, 1407–1414. [[CrossRef](#)]
18. Takahashi, M. Development of high strength steels for automobiles. *Nippon Steel Tech. Rep.* **2003**, *88*, 2–7.
19. Pornputsiri, N.; Kanlayasiri, K. Effect of bending temperatures on the microstructure and springback of a TRIP steel sheet. *Def. Technol.* **2020**, *16*, 980–987. [[CrossRef](#)]
20. Barnwal, V.K.; Lee, S.; Yoon, S.; Kim, J.; Barlat, F. Fracture characteristics of advanced high strength steels during hole expansion test. *Int. J. Fract.* **2020**, *224*, 217–233. [[CrossRef](#)]
21. Sugimoto, K.; Kanda, A.; Kikuchi, R.; Hashimoto, S.; Kashima, T.; Ikeda, S. Ductility and formability of newly developed high strength low alloy TRIP-aided sheet steels with annealed martensite matrix. *ISIJ Int.* **2002**, *42*, 910–915. [[CrossRef](#)]
22. Sugimoto, K.; Hojo, T.; Nagasaka, A.; Hashimoto, S.; Ikeda, S. The effects of Nb and Mo additions on the microstructure and formability of C-Mn-Si-Al TRIP-aided ferrous sheet steels with an annealed martensite matrix. *Steel Grips* **2004**, *2*, 483–487.
23. De Cooman, B.C.; Kwon, O.; Chin, K. State-of-the-knowledge on TWIP steel. *Mater. Sci. Technol.* **2012**, *28*, 513–527. [[CrossRef](#)]
24. Gwon, H.; Kim, J.; Kim, J.; Suh, D.; Kim, S. Role of grain size on deformation microstructures and stretch-flangeability of TWIP steel. *Mater. Sci. Eng. A* **2020**, *773*, 138861. [[CrossRef](#)]
25. Paul, S.K. A critical review on hole expansion ratio. *Materialia* **2020**, *9*, 100566. [[CrossRef](#)]
26. Kobayashi, J.; Pham, D.V.; Sugimoto, K. Stretch-flangeability of 1.5 GPa grade TRIP-aided martensitic cold rolled sheet steels. In Proceedings of the 10th International Conference on Technology of Plasticity (ICTP 2011), Aachen, Germany, 25–30 September 2011; pp. 598–603.
27. Sugimoto, K.; Sakaguchi, J.; Iida, T.; Kashima, T. Stretch-flangeability of a high-strength TRIP type bainitic sheet steel. *ISIJ Int.* **2000**, *40*, 920–926. [[CrossRef](#)]
28. Polatids, E.; Haidemenopoulos, G.N.; Krizan, D.; Aravas, N.; Panzner, T.; Šmíd, M.; Papadioti, I.; Casati, N.; Van Petegem, S.; Van Swygenhoven, H. The effect of stress triaxiality on the phase transformation in transformation induced plasticity steels: Experimental investigation and modelling the transformation kinetics. *Mater. Sci. Eng. A* **2021**, *800*, 140321. [[CrossRef](#)]
29. Wang, Y.; Xu, Y.; Wang, Y.; Zhang, J.; Guo, C.; Wang, X.; Zhao, W.; Liu, H. Enhanced stretch flangeability and crack propagation behavior of an 1100 MPa grade TRIP aided bainitic ferrite steel. *J. Mater. Res. Technol.* **2023**, *26*, 5503–5517. [[CrossRef](#)]
30. Jiang, H.; He, Y.; Lin, L.; Zhang, Y.; Zheng, W.; Li, L. Microstructures and properties of auto-tempering ultra-high strength automotive steel under different thermal-processing conditions. *Metals* **2021**, *11*, 1121. [[CrossRef](#)]
31. Tang, S.; Lan, H.; Liu, Z.; Wang, G. Enhancement of balance in strength, ductility and stretch flangeability by two-step austempering in a 1000 MPa grade cold rolled bainitic steel. *Metals* **2021**, *11*, 96. [[CrossRef](#)]
32. Huyghe, P.; Dépinoy, S.; Caruso, M.; Mercier, D.; Georges, C.; Malet, L.; Godet, S. On the effect of Q&P processing on the stretch-flange-formability of 0.2C ultra-high strength steel sheets. *ISIJ Int.* **2018**, *58*, 1341–1350.
33. Im, Y.; Kim, E.; Song, T.; Lee, J.; Suh, D. Tensile properties and stretch-flangeability of TRIP steels produced by quenching and partitioning (Q&P) process with different fractions of constituent phases. *ISIJ Int.* **2021**, *61*, 572–581.

34. Xia, P.; Vercruyse, F.; Celada-Casero, C.; Verleysen, P.; Petrov, R.H.; Sabirov, I.; Molina-Aldareguia, J.M.; Smith, A.; Linke, B.; Thiessen, R.; et al. Effect of alloying and microstructure on formability of advanced high-strength steels processed via quenching and partitioning. *Mater. Sci. Eng. A* **2022**, *831*, 142217. [[CrossRef](#)]
35. Toji, Y.; Nakagaito, T.; Matsuda, H.; Hasegawa, K.; Kaneko, S. Effect of microstructure on mechanical properties of quenching and partitioning steel. *ISIJ Int.* **2023**, *63*, 758–765. [[CrossRef](#)]
36. Sugimoto, K.; Hidaka, S.; Tanino, H.; Kobayashi, J. Warm formability of 0.2 pct C-1.5 pct Si-5 pct Mn transformation-induced plasticity-aided steel. *Metall. Mater. Trans. A* **2017**, *48*, 2237–2246. [[CrossRef](#)]
37. Kim, j.; Kwon, M.; Lee, J.; Lee, S.; Lee, K.; Suh, D. Influence of isothermal treatment prior to initial quenching of Q&P process on microstructure and mechanical properties of medium Mn steel. *ISIJ Int.* **2021**, *61*, 518–526.
38. Iwata, K.; Ueda, K.; Yamada, Y. Study of shearing mechanism based on direct SEM observation. *J. Jpn. Soc. Technol. Plast.* **1979**, *20*, 437–443. (In Japanese)
39. Sugimoto, K.; Shioiri, S.; Kobayashi, J. Effects of mean normal stress on strain-hardening, strain-induced transformation, and void-formation behaviors of high-strength TRIP-aided steels. *Metals* **2024**, *14*, 61. [[CrossRef](#)]
40. Maruyama, H. X-ray measurement of retained austenite. *Jpn. Soc. Heat Treat.* **1977**, *17*, 198–204. (In Japanese)
41. Dyson, D.J.; Holmes, B. Effect of alloying additions on the lattice parameter of austenite. *J. Iron Steel Inst.* **1970**, *208*, 469–474.
42. Cullity, B.D. *Elements of X-ray Diffraction*, 2nd ed.; Addison-Wesley Publishing Company, Inc.: Boston, MA, USA, 1978; p. 287.
43. Williamson, G.K.; Hall, W.H. X-ray line broadening from filed aluminum and wolfram. *Acta Metall.* **1953**, *1*, 22–31. [[CrossRef](#)]
44. Takebayashi, S.; Kunieda, T.; Yoshinaga, N.; Ushioda, K.; Ogata, S. Comparison of the dislocation density in martensitic steels evaluated by some X-ray diffraction methods. *ISIJ Int.* **2010**, *50*, 875–882. [[CrossRef](#)]
45. Mura, T.; Mori, T. *Micromechanics*; Baifukan Co., Ltd.: Tokyo, Japan, 1976; p. 23. (In Japanese)
46. Sakaki, T.; Sugimoto, K.; Fukuzato, T. Role of internal stress for continuous yielding of dual-phase steels. *Acta Metall.* **1983**, *31*, 1737–1746. [[CrossRef](#)]
47. Ashby, M.F. Work hardening of dispersion-hardened crystals. *Philos. Mag.* **1966**, *14*, 1157–1178. [[CrossRef](#)]
48. Kobayashi, J.; Ina, D.; Futamura, A.; Sugimoto, K. Fracture toughness of an advanced ultrahigh-strength TRIP-aided steel. *ISIJ Int.* **2014**, *54*, 955–962. [[CrossRef](#)]

**Disclaimer/Publisher’s Note:** The statements, opinions and data contained in all publications are solely those of the individual author(s) and contributor(s) and not of MDPI and/or the editor(s). MDPI and/or the editor(s) disclaim responsibility for any injury to people or property resulting from any ideas, methods, instructions or products referred to in the content.